

Catalogue of wide binary, trinary and quaternary candidates from the Gaia data release 2 (region $|b| > 25$ deg)

PETR ZAVADA¹ AND KAREL PÍŠKA¹

¹*Institute of Physics of the Czech Academy of Sciences, Na Slovance 2, 182 21 Prague 8, Czech Republic*

(Accepted by the Astronomical Journal: October, 2021)

ABSTRACT

The occurrence of multiple stars, dominantly binaries, is studied using the *Gaia*-ESA DR2 catalogue. We apply the optimized statistical method that we previously developed for the analysis of 2D patterns. The field of stars is divided into a mosaic of small pieces, which represent a statistical set for analysis. Specifically, data input is represented by a grid of circles (events) with radius 0.02 deg covering the sky in the field of galactic latitude $|b| > 25$ deg. The criteria for selecting candidates for multiple stars are based on two parameters: angular separation and collinearity of proper motion. Radial separation, due to limited accuracy, is used only as a weaker supplementary constraint. Due attention is paid to the accurate calculation of the background, which is a necessary input for evaluating the quality of the candidates. Our selection algorithm generates the catalogue of candidates: 900,842 binaries, 5,282 trinaries and 30 quaternaries.

1. INTRODUCTION

It is believed that statistics of binaries and multiple stars can provide deeper insights into the formation and evolution of galaxies. Wide binaries may serve as a sensitive probe of the Galactic gravitational potential. Some recent studies suggest that very wide binaries may provide data on the presence of dark matter in the Galaxy (Peñarrubia et al. (2016); Hernandez et al. (2019); Pittordis&Sutherland (2019)). At present, an extremely rich source of data on stars of our Galaxy is provided by the *Gaia*-ESA mission and collected in the catalogue DR2 (Gaia Collaboration (2018)). The release of the next and more expanded full version (DR3) is expected in the first half of 2022. Several authors have recently studied various aspects of binaries using the *Gaia* DR1 (Oelkers et al. (2017); Oh et al. (2017)), DR2 (Ziegler et al. (2018); El-Badry&Rix (2018); Godoy-Rivera (2018); Jiménez-Esteban et al. (2019); González-Santamaría et al. (2020); Sapozhnikov et al. (2020); Hartman&Lépine (2020); Tian et al. (2020)) and EDR3 (Early Data Release 3) (El-Badry et al. (2021); Gaia Collaboration (2021)) catalogues. Other important articles examining wide binaries before *Gaia* include, for example, Cabalero (2009) and Close et al. (1990).

In our previous study (Zavada&Píška (2018, 2020)) we have developed and applied statistical methods for the identification of binaries and multiple stars with an accurate estimate of the background. The resulting catalogue is based on the 3D event analysis and contains about 8×10^4 binary candidates at a distance of up to $\lesssim 340$ pc. This catalogue involves the binary stars whose total separation does not exceed the event sphere diameter that was 4 pc. Because determining the radial separation Z_{ij} can have a significant error, we have been selecting the binary stars in the events based on the distribution of the projected distances Δ_{ij} , the error of which is only slightly affected by the parallax error. At the same time, the error of parallax and radial distance causes that the constraint on radial separation $Z_{ij} \leq 4$ pc can exclude a large number of true binary stars. In the present study, we solve this drawback of 3D events by a more general procedure. The procedure combines the analysis of angular separations d_{ij} of sources inside 2D events with the information on the radial separation Z_{ij} . Simultaneously, we apply the condition of approximate collinearity of proper motion here as before. The result of the procedure is the selection of candidates for the binary with the defined probability that it is the true binary and not a random background.

Our 2D analysis is described in Sec.2 and consists of several parts. The basic notions, which our method deals with are defined in section 2.1. Input data from the sector of the *Gaia* catalogue are defined in section 2.2. In the next section 2.3 we analyze the probability of the binary depending on the angular separation and collinearity of proper motion of its components. This analysis sets the rules for the selection of binary candidates for our new catalogue.

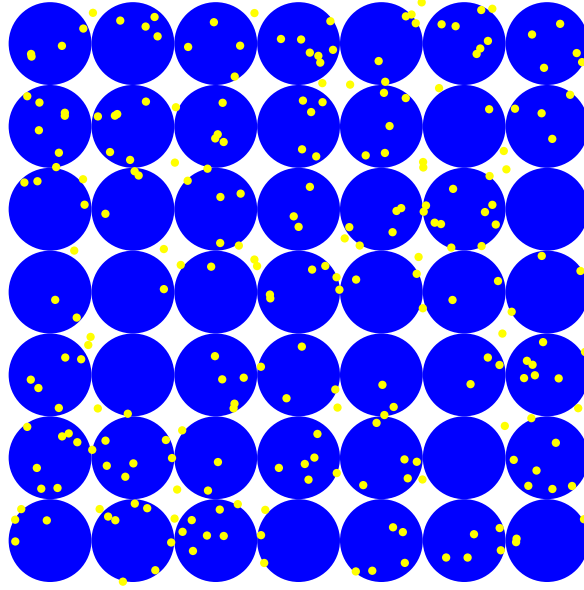


Figure 1. Grid of 2D event circles with uniform distribution of the stars.

Using parallax, we can define the distance of binary and the projection of the absolute separation, which is more important for physics than just the angular separation. In section 2.4 we show that distributions of the projection and correlations with proper motion allow us to obtain information about binary orbit. In section 2.5 we show the results of our analysis on the occurrence of trinaries and quaternaries. Candidates with a high degree of reliability are listed in the electronic catalogue. Its structure and content are described in Sec.3. The comparison with the other catalogues (El-Badry et al. (2021); Hartman&Lépine (2020); Jiménez-Esteban et al. (2019); Zavada&Píška (2020)) is done in Sec.4. The last Sec.5 is devoted to the summary and concluding remarks.

2. STATISTICAL ANALYSIS OF 2D PATTERNS

2.1. Methodology

The method of 2D analysis is described in detail in our previous paper Zavada&Píška (2020), so here we repeat only basic notions.

The data for analysis are represented by the grid of circles with patterns of stars covering a defined region of sky (Fig.1). The input data for generating the grid are given in the galactic reference frame. So, the position \mathbf{L} of a source is defined by spherical coordinates L, l and b (distance from the Sun, galactic longitude and latitude):

$$\begin{aligned} \mathbf{L} &= L\mathbf{n}; \quad \mathbf{n} = (\cos b \cos l, \cos b \sin l, \sin b), \\ -\frac{\pi}{2} &\leq b \leq \frac{\pi}{2}, \quad -\pi < l \leq \pi. \end{aligned} \quad (1)$$

In the centre of each circle we define local orthonormal frame defined by the basis:

$$\begin{aligned} \mathbf{k}_r &= \mathbf{n}_0 = (\cos b_0 \cos l_0, \cos b_0 \sin l_0, \sin b_0), \\ \mathbf{k}_l &= (-\sin l_0, \cos l_0, 0), \\ \mathbf{k}_b &= (-\sin b_0 \cos l_0, -\sin b_0 \sin l_0, \cos b_0), \end{aligned} \quad (2)$$

where $\mathbf{k}_r = \mathbf{n}_0(b_0, l_0)$ defines angular position of the circle centre. Unit vector \mathbf{k}_l is perpendicular to \mathbf{k}_r and has direction of increasing l . Unit vector \mathbf{k}_b is defined as $\mathbf{k}_b = \mathbf{k}_r \times \mathbf{k}_l$ and has direction of increasing b . Vector \mathbf{k}_r has radial direction, perpendicular vectors \mathbf{k}_b and \mathbf{k}_l lies in the transverse plain. The stars inside the circle of small radius ρ_2 satisfy

$$|\mathbf{n}_i - \mathbf{n}_0| \leq \rho_2, \quad i = 1, \dots, M. \quad (3)$$

	2D region: $l \times b[\text{deg}^2]$	$\rho_2[\text{as}]$	$\langle L \rangle [\text{pc}]$	$\langle M \rangle$	N_e	N_s	N_{tot}
R ₁	$\langle -180, 180 \rangle \times \langle \pm 45, \pm 90 \rangle$	72	1,807	3.86	5,887,737	22,083,670	30,643,238
R ₂	$\langle -180, 180 \rangle \times \langle \pm 25, \pm 45 \rangle$	72	2,134	7.86	6,985,043	53,043,629	80,653,496

Table 1. Analyzed regions $\mathbf{R}_{1,2}$ in the DR2 catalogue, where ρ_2 is the angular radius of the events, $\langle L \rangle, \langle M \rangle$ are average distance and event multiplicity, N_e is the total number of events. Only sources with positive parallax and in distance $< 15,000 \text{ pc}$ are taken into account and only events $2 \leq M \leq 25$ are accepted for present analysis. N_s is number of sources after these cuts, N_{tot} is total number of sources with positive parallax in $\mathbf{R}_{1,2}$.

or

$$\{x_i, y_i\}; \quad x_i^2 + y_i^2 \leq \rho_2^2, \quad i = 1, \dots, M, \quad (4)$$

where $\{x_i, y_i\}$ are local rectangular coordinates defined by the basis (2):

$$x_i = \mathbf{n}'_i \cdot \mathbf{k}_l, \quad y_i = \mathbf{n}'_i \cdot \mathbf{k}_b; \quad \mathbf{n}'_i = \mathbf{n}_i - \mathbf{n}_0. \quad (5)$$

The circles in the grid are, in fact, spherical caps. However, their radius ρ_2 will be so small ($\simeq 3.5 \times 10^{-4} \text{ rad}$), that the caps can be reliably considered as flat circles.

A set of stars defined by (4) is called the *event*. We define the pair separations

$$x_{ij} = |x_j - x_i|; \quad y_{ij} = |y_j - y_i|; \quad d_{ij} = \sqrt{x_{ij}^2 + y_{ij}^2}; \quad i, j = 1, 2, \dots, M. \quad (6)$$

It is useful to define the scaled separation

$$\hat{\xi} = \frac{d_{ij}}{2\rho_2}; \quad 0 \leq \hat{\xi} \leq 1, \quad (7)$$

where ρ_2 is the angular radius of the events. Distribution of separations of randomly distributed sources inside the circle *does not depend* on M and is given by relation

$$q(\hat{\xi}) = \frac{16\hat{\xi}}{\pi} \left(\arccos \hat{\xi} - \hat{\xi} \sqrt{1 - \hat{\xi}^2} \right), \quad (8)$$

which was proved in (Zavada&Pířka (2020)). This curve is important for subtraction of random background.

Before practical use, we add a few general remarks:

i) Of course, the grid in Fig.1 can be rectangular only locally. In fact, we work with circles with the same radius aligned only in rows with a constant galactic latitude.

ii) The radius ρ_2 must be set to be significantly larger than a typical separation of true binary. At the same time, it must be so small that the distribution of stars within the event can be considered random and uniform. In Sec. 2.3 these conditions will be explained in more detail. We will also explain that the obtained results are not sensitive to the exact setting of ρ_2 .

iii) Events with too high multiplicity M , in which various higher dense structures may dominate, are excluded from processing.

iv) The circular shape of the events is chosen due to a simple but accurate formula (8) for calculating a random background. Another shape would lead to a more complex formula depending on other shape parameters (triangle, square, orientation ...). On the other hand, the grid of circle events only partially covers the sky. The complete set of binaries is obtained in Sec.3 from several shifted grids.

2.2. Input data

The parameters of the events we work with are listed in Tab.1. By symbol \mathbf{R} we denote the union of both regions in table:

$$\mathbf{R} = \mathbf{R}_1 \cup \mathbf{R}_2. \quad (9)$$

In Fig.2 we have shown distribution of the distances of the stars in the table from the Sun (origin of the galactic reference frame). If the parallax p is given in angular units **as** ($= 1''$), then the corresponding distance is

$$L[\text{pc}] = \frac{1}{p[\text{as}]} \quad (10)$$

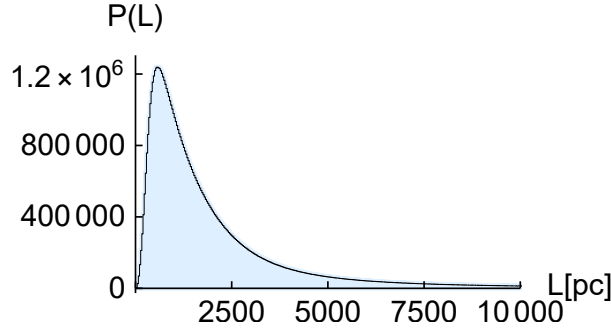


Figure 2. Distribution of distances of stars of the region **R**. Binning: 30pc.

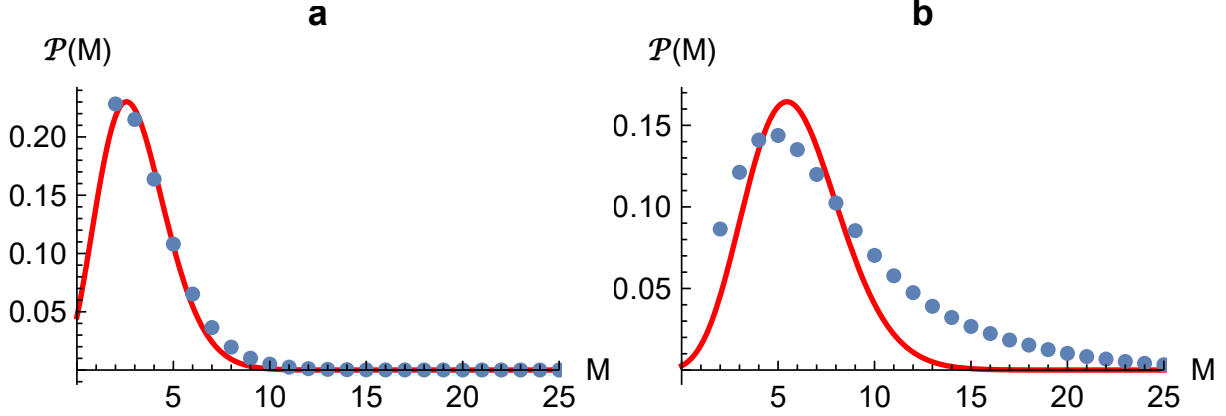


Figure 3. Distribution of multiplicities of events from regions **R**₁ (panel *a*) and **R**₂ (panel *b*). Red curves represent Poisson distributions, where discrete values $M!$ are interpolated by gamma function $\Gamma(M + 1)$.

The figure demonstrates the scale of distances measured by *Gaia*. This histogram also suggests the convention valid for all histograms $P(x)$ in this paper: ordinate represents the number of entries of variable x of given value into the bins of the width specified in the figure caption.

Stars in the sky are divided into the circle regions (events) of angular radius ρ_2 and in Fig.3 we show distribution of the star multiplicities in these events. The distribution of stars in region **R**₁ is roughly homogenous, so the multiplicity distribution has a nearly Poisson shape

$$\mathcal{P}(M) = \frac{\lambda^M}{M!} \exp(-\lambda); \quad \lambda = \langle M \rangle. \quad (11)$$

Since region **R**₂ shows greater density fluctuations resulting in a broader distribution than Poisson, we fail to make its fit. This region is dominated by an inhomogeneous stellar density due to patchy inter-stellar extinction, the presence of open clusters, and the imprint of the Galactic spiral pattern.

The proper motion of the stars in DR2 is defined by two angular velocities

$$\mu_\alpha^* (\equiv \mu_\alpha \cos \delta), \quad \mu_\delta \quad (12)$$

in directions of the right ascension and declination in the ICRS. So the corresponding transverse 2D velocity **U** is given as

$$\mathbf{U} = L\mathbf{u}, \quad \mathbf{u} = (\mu_\alpha^*, \mu_\delta), \quad u = |\mathbf{u}|. \quad (13)$$

For the pair of stars we can define the angle between both transverse velocities:

$$\alpha_{ij} = \arccos \frac{\mathbf{u}_i \cdot \mathbf{u}_j}{u_i u_j}. \quad (14)$$

Our selection of binaries is based on Fig.4 obtained from all events in the table. The peak in the domain of small

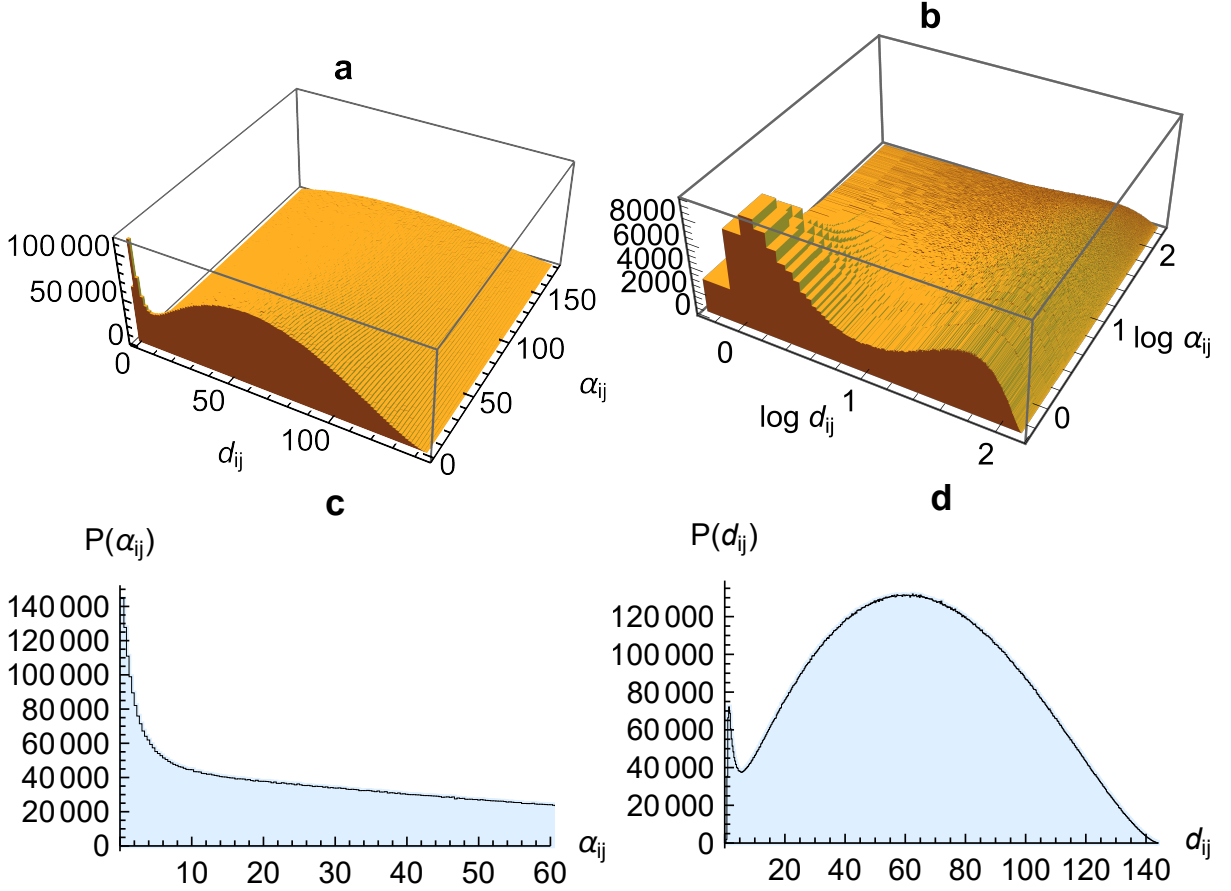


Figure 4. Signature of binaries in region **R**: distribution $P(d_{ij}, \alpha_{ij})$ (panels *a, b* - linear and logarithmic scales), distribution $P(\alpha_{ij})$ for $d_{ij} \leq 15$ as (panel *c*) and distribution $P(d_{ij})$ for $\alpha_{ij} \leq 15$ deg (panel *d*). Units: d_{ij} [as], α_{ij} [deg]. Binning: $1.44\text{as} \times 1.8$ deg, $0.36\text{as} \times 0.45$ deg, 0.36 deg, 0.288as .

separations d_{ij} and small angles α_{ij} represents a clear signature of binaries (panel *a*). The domain of the peak can be approximately defined by the conditions

$$d_{ij} \leq 15 \text{ as}, \quad \alpha_{ij} \leq 15 \text{ deg}. \quad (15)$$

The second condition was applied also in our former 3D analysis. Panel *b* shows distribution $P(\alpha_{ij})$ in the band $d_{ij} \leq 15$ as, similarly in panel *c* we have distribution $P(d_{ij})$ for $\alpha_{ij} \leq 15$ deg. Recall that the stars separated by $d_{ij} \lesssim 0.5$ as are missing due to current resolution limit in the DR2 data set as stated in (Arenou et al. (2018)).

In Fig.5 we have shown distribution of radial separations Z_{ij} defined as

$$Z_{ij} = |L_i - L_j| \quad (16)$$

and obtained with the use of parallax (10). Panel *a(b)* shows distribution of pairs outside (inside) the window (15). The sharp peak at small radial separations in the second panel is expected for binaries, the tail with greater separations corresponds partly to the background pairs and partly to the true binaries having large errors of parallaxes. Alternative distributions $P(\Delta L/L)$, where

$$\Delta L \approx Z_{ij}, \quad L = \frac{L_i + L_j}{2}, \quad (17)$$

are shown in Fig.6*a, b*. Relation (10) implies

$$\frac{\Delta L}{L} \approx \frac{\Delta p}{p}. \quad (18)$$

In Fig.6*c* we show distribution $P(\Delta p/p)$ obtained directly from the *Gaia* data, where the parallax of the source is accompanied by its estimated error. Our $\Delta L, L$ related to binaries are also obtained from parallaxes, however, our

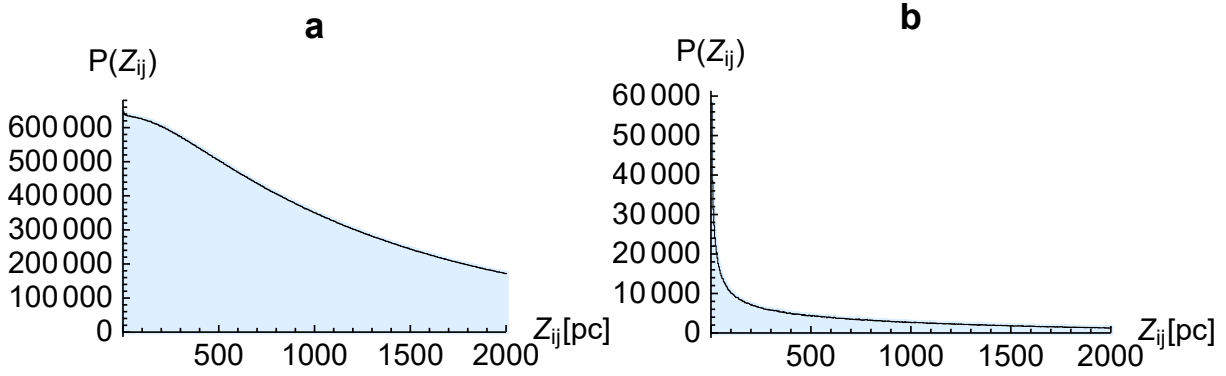


Figure 5. Radial separations for pairs of the region **R** outside window (15) (panel *a*) and inside the window (panel *b*). Binning: 4pc.

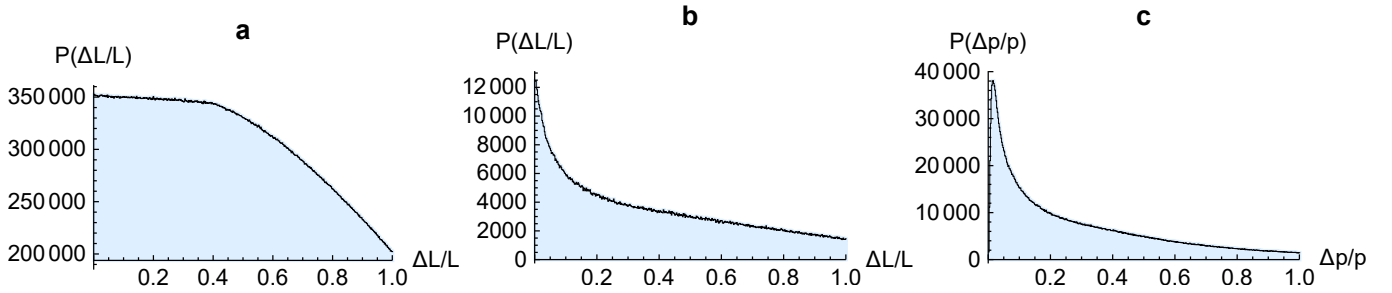


Figure 6. Comparison of distributions of relative errors: $\Delta L/L$ outside (panel *a*), inside (panel *b*) the window of binaries (15) and $\Delta p/p$ (panel *c*) for sources inside the window. Data are from the region **R**. Binning: 0.002.

estimate of relative error of the parallax is independent and can serve as a cross-check. We observe a noticeable similarity between the distributions *b,c*. A smaller difference can arise because the window of binaries also contains a background with random radial separations.

2.3. Selection of binaries and calculation of background

In the next we will work with the numbers:

n_2 — number of (true) binaries

b_2 — number of background pairs

N_2 — total number of pairs:

$$N_2 = n_2 + b_2. \quad (19)$$

These numbers are related to given sample of pairs defined by the corresponding cuts. One cannot decide if the pair is a binary or background, but we can find out the probability that the pair is binary (n_2/N_2) or background (b_2/N_2). Obviously, in the domain of the peak in Fig.4*a* the probability of binaries n_2/N_2 is high.

Radial separation Z_{ij} can be used to further increase the probability of binaries in the peak, but due to low accuracy, the cut must be set judiciously. Too strict cut generates a cleaner sample of binaries (higher ratio n_2/N_2) but more binaries are excluded. And conversely, too soft cut preserves more binaries, but at the price of the higher background and lower ratio n_2/N_2 .

The area $d \times \alpha$ of Fig.4*a* can be divided into four the windows **A,B,C** and **D** (like in Fig.8):

$$\mathbf{A} = \langle 0, d_c \rangle \times \langle 0, \alpha_c \rangle; \quad d_c = 15 \text{ as}, \quad \alpha_c = 15 \text{ deg}, \quad (20)$$

which is the domain of the peak (15) with the high population of binaries. The remaining windows are

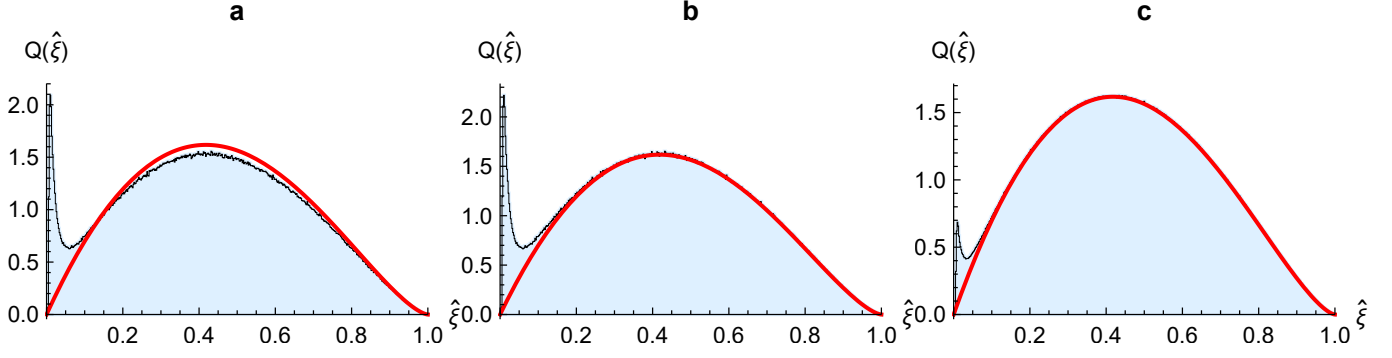


Figure 7. Scaled separation $\hat{\xi}$: the peak of binaries and random background (*red curve*). Region \mathbf{R}_1 : equal normalization of data and background (panel *a*), data and renormalized background (panel *b*). Region \mathbf{R}_2 : data and renormalized background (panel *c*).

$$\begin{aligned} \mathbf{B} &= \langle d_c, d_{\max} \rangle \times \langle 0, \alpha_c \rangle, \\ \mathbf{C} &= \langle d_c, d_{\max} \rangle \times \langle \alpha_c, 180 \rangle, \\ \mathbf{D} &= \langle 0, d_c \rangle \times \langle \alpha_c, 180 \rangle. \end{aligned} \quad (21)$$

Distribution $P(d_{ij})$ can be represented by its normalized form

$$Q(\hat{\xi}) = \frac{1}{N_2} P(d_{ij}); \quad \hat{\xi} = \frac{d_{ij}}{2\rho_2}. \quad (22)$$

The random background is described by the normalized function $q(\hat{\xi})$ defined by Eq.(8). Both distributions are shown in Fig.7*a* for region \mathbf{R}_1 . Due to equal normalization, an excess in the peak of binaries in distribution P is compensated by the lack of pairs in the region of background. Assuming that for $d_{ij} \geq 2/3 d_{\max}$ or $\hat{\xi} \geq 2/3$ distribution P involves only background, we renormalize q correspondingly:

$$q(\hat{\xi}) \rightarrow q^r(\hat{\xi}) = \gamma q(\hat{\xi}); \quad \gamma = \frac{\int_{\hat{\xi} \geq 2/3} Q(\hat{\xi}) d\hat{\xi}}{\int_{\hat{\xi} \geq 2/3} q(\hat{\xi}) d\hat{\xi}}. \quad (23)$$

In panel *b* we have shown distribution $Q(\hat{\xi})$ together with the renormalized background $q^r(\hat{\xi})$. The same distributions for region \mathbf{R}_2 is shown in panel *c*. Obviously, the distribution of binaries is given by their difference

$$P_{bin}(\hat{\xi}) = N_2 \left(Q(\hat{\xi}) - q^r(\hat{\xi}) \right). \quad (24)$$

It is now clear from these figures why the diameter of events $2\rho_2$ is chosen much greater than typical separation of the binaries d_{bin} (the parameter $\hat{\xi}_{bin} = d_{bin}/2\rho_2 \lesssim 0.1$ in the figures). The larger diameter allows us to more accurately determine the weight of the background curve to be subtracted. At the same time we observe the distribution of separations is perfectly random outside the region of binary peak.

The probability that the pair in the event is the true binary and not a random background is given by the ratio

$$\beta(\hat{\xi}) = \frac{P_{bin}(\hat{\xi})}{N_2 Q(\hat{\xi})} = 1 - \frac{\gamma q(\hat{\xi})}{Q(\hat{\xi})}, \quad (25)$$

where one can replace $\hat{\xi} \rightarrow d_{ij} = 2\rho_2 \hat{\xi}$. Examples of the function β will be given below. The shape of the background distribution q depends on $\hat{\xi}$ only. In the background, we can see an increase or peak at low $\hat{\xi}$, which is a signal of the presence of binaries. An additional selection of pairs with small α_{ij} or a small radial separation Z_{ij} increases the dimension of the peak on the background, but the shape of the background curve does not change. For instance, Fig.7*b,c* corresponds to $\alpha_{ij} \leq 15^\circ$. The reason is simple: in the sky without binaries (only background can be observed) there is no correlation between angular separation d_{ij} and the parameters α_{ij} or Z_{ij} .

$l[\text{deg}]$	$\langle -30, +30 \rangle$	$\langle \pm 30, \pm 90 \rangle$	$\langle 90, 270 \rangle$
$\Delta L_{\text{max}}[\text{pc}]$	50	100	400

Table 2. Cuts on radial separation in galactic longitude subregions of region **R**₂.

From the data we have known the numbers of pairs in four windows defined above: N_2^A, N_2^B, N_2^C and N_2^D . The number N_2^A is called the number of binary candidates. According to an assumption above, we have also numbers of background pairs obtained for $\hat{\xi} \geq 2/3$ in domains

$$\langle 0, \alpha_c \rangle \rightarrow N_2^I, \quad \langle \alpha_c, 180 \rangle \rightarrow N_2^{II}. \quad (26)$$

If we denote

$$w(x) = \int_x^1 q(\hat{\xi}) d\hat{\xi}, \quad (27)$$

then we can calculate the numbers of background pairs in the windows **A-D** as

$$\begin{aligned} b_2^A &= N_2^I \frac{1 - w(d_c)}{w(2/3)}, & b_2^B &= N_2^I \frac{w(d_c)}{w(2/3)}, \\ b_2^C &= N_2^{II} \frac{w(d_c)}{w(2/3)}, & b_2^D &= N_2^{II} \frac{1 - w(d_c)}{w(2/3)}. \end{aligned} \quad (28)$$

Therefore, the numbers of binaries in the respective windows read

$$\begin{aligned} n_2^A &= N_2^A - b_2^A, & n_2^B &= N_2^B - b_2^B, \\ n_2^C &= N_2^C - b_2^C, & n_2^D &= N_2^D - b_2^D. \end{aligned} \quad (29)$$

These numbers, obtained in both regions **R**₁ and **R**₂ under different conditions are given in Fig.8. The numbers in upper panels **A, B** (the set All events) follow from panels *b, c* in Fig.7. The peaks of binaries are evident, however the area under the background curve is also considerable. Correspondingly, the quality ratios $\beta^A = n_2^A/N_2^A$ (in the second row of the panels **A**), representing the probability of the true binary in window **A** are not satisfactory, particularly for the region **R**₂. Parameter β^A can be increased by applying the additional cut on radial separation ΔL . The condition

$$\Delta L \leq \Delta L_{\text{max}} = 500 \text{ pc} \quad (30)$$

applied in the region **R**₁ gives “enriched” sample with the quality ratio $\beta^A = 0.77$ (left middle panel). In the region **R**₂ the situation is more complicated. The density of stars is higher, so the background grows. Moreover, the average density varies with longitude. So, we have divided the region into three subregions with different ΔL_{max} cuts, which give a similar β^A in these subregions. Their definition is shown in Tab.2. These cuts give resulting β^A and other parameters related to **R**₂ listed in right middle panel. One could further squeeze the cuts to obtain a cleaner sample of binaries (higher ratio n_2^A/N_2^A), however at the price that more true binaries are excluded (n_2^A is smaller). This is illustrated by the numbers in upper and middle yellow panels in the figure. The cuts exclude not only background pairs but also true binaries in window **A**. It is due to a rather poor accuracy of radial separation that we have shown in Fig.5*b*. If we had an accurate radial separation, then a suitable cut would suppress only background and preserve true binaries.

The situation is more favorable with brighter stars. The lower panels in Fig.8 show that for binaries of magnitude $G \leq 15$ the quality ratio β^A is very good even without any cut on radial separation. The quality of this sample is illustrated also by Fig.9, where we observe the high binary peaks with low background. In any case, our criterion is based on the resulting ratio β^A , so we can accept candidates with greater parallax uncertainty if β^A is greater than requested. In other words, if the signature from d_{ij} and α_{ij} is sufficient, then the parallax is not important.

Equivalently, abundance of binaries depending on their separation is defined by β function (25). In Fig.10*a, b, c* we have shown this function for some subsets of regions **R**₁ and **R**₂ defined by Fig.8. Figure Fig.10 demonstrates that higher β^A could be also reached by squeezing the parameter d_c in window **A** (20). Note, the effectively wider peak for magnitude $G \leq 15$ is due to a lower level of background pairs, which can be seen from the comparison of Fig.9 with Fig.7*b, c*.

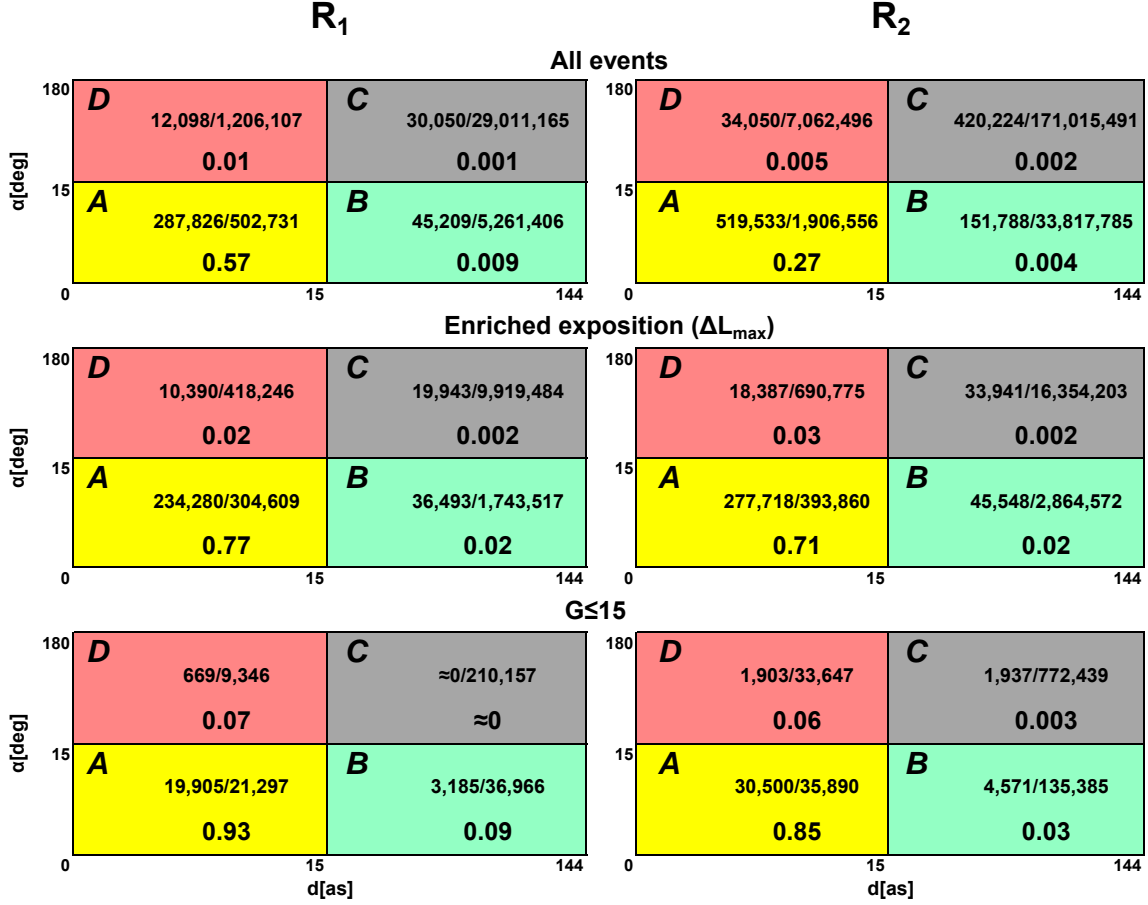


Figure 8. Ratio n_2/N_2 of the number of binaries and the total number of pairs in different $d \times \alpha$ windows in the regions R_1 and R_2 under different conditions. The result of this ratio (β) is in the second row of the respective window.

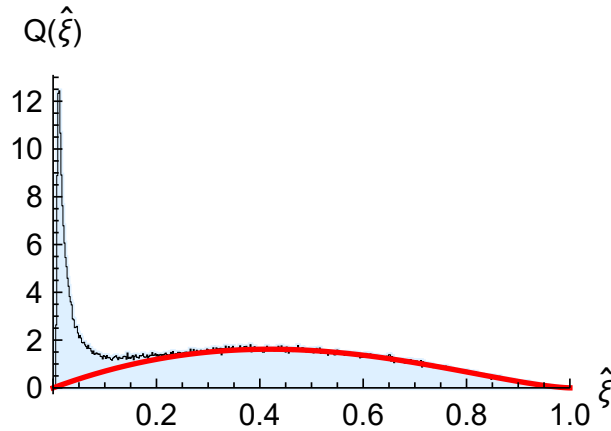


Figure 9. Scaled separation $\hat{\xi}$: peak of binaries of magnitude $G \leq 15$ and random background (red curve) in region R .

We have shown that the function β is a key to determining the quality and quantity of binaries in the selected subset. It is, therefore, necessary to verify that this function does not change with the choice of the purely technical parameter ρ_2 . Fig.10d shows the function β calculated for the sub-sample of enriched exposition with event radius

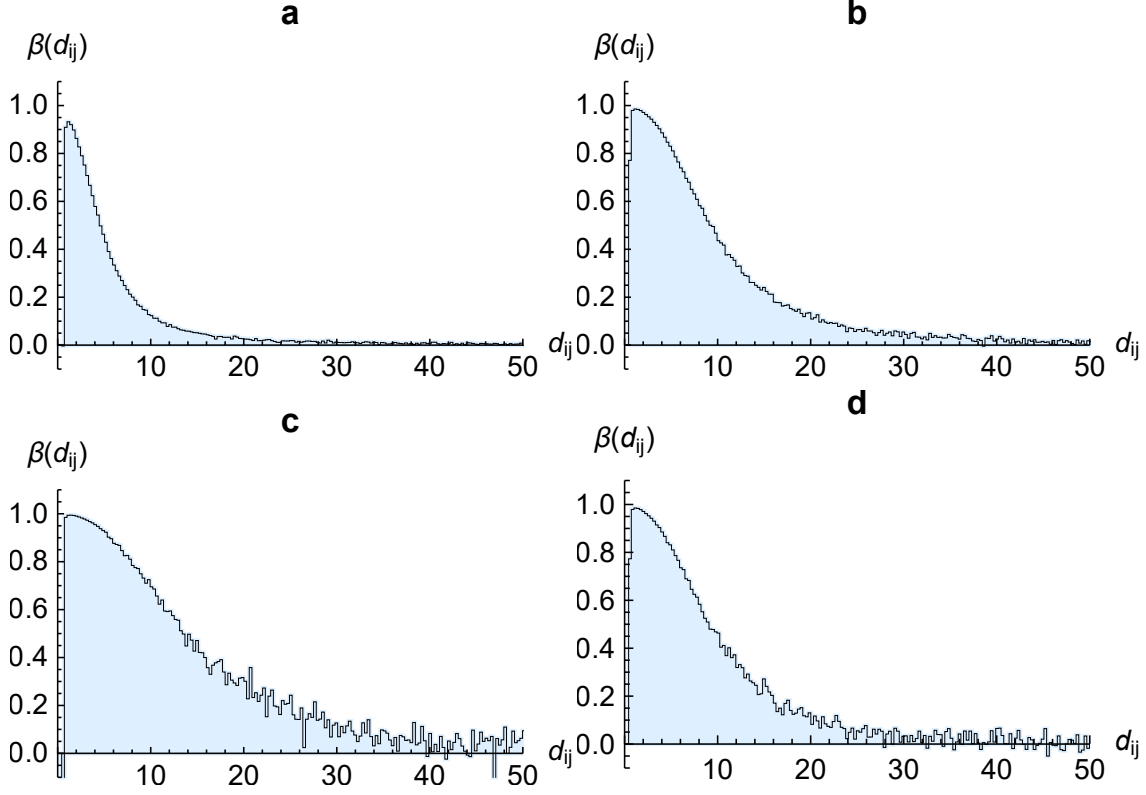


Figure 10. Function β defines probability of true binary at different separations in \mathbf{R} for $\alpha \leq \alpha_c$. Panel *a*: all events. Panel *b*: enriched exposition. Panel *c*: only stars of magnitude $G \leq 15$. Panel *d*: enriched exposition, event subsample $\rho_2 = 36\text{as}$. Unit: $d_{ij}[\text{as}]$.

$\rho_2 = 36\text{as}$ (half the radius of standard events). The functions in panels *b, d* agree perfectly. A similar agreement was also verified for Figs.12 - 14 below.

What is the effect of input data uncertainties on the selection quality? The initial distribution $P(d_{ij}, \alpha_{ij})$ in Fig.4 consists of two parts

$$P(d_{ij}, \alpha_{ij}) = P_{bin}(d_{ij}, \alpha_{ij}) + P_{bg}(d_{ij}, \alpha_{ij}), \quad (31)$$

corresponding to the true binaries and the background. The shape of the distribution $P_{bin}(d_{ij}, \alpha_{ij})$ is affected by the measurement errors. In general, these errors cause a widening of this distribution, but its integral n_2 does not change, as suggested in Fig.11. However, the errors will affect the value of the quality ratio

$$\beta^P = \frac{n_2}{n_2 + b_2} \quad (32)$$

in the domain of the peak. As suggested in the figure, wider P_{bin} means larger b_2 , which implies a smaller ratio β^P . In this way, the measurement errors of the selection parameters directly affect the β function, larger errors mean worse β . At the same time, larger errors expand the space for selection. A similar result follows from the algorithm in (Halbwachs (1986)) for the selection of common proper motion pairs.

At the end of this section, we summarize the selection algorithm of binary candidates:

1. In the distribution $P(d_{ij}, \alpha_{ij})$ in Fig.4 we observe the peak on a smooth background. The peak is a sign of the presence of binaries. We take the edges (15) of this peak as the limits of our selection of binary candidates.

2. The number of true binaries can be accurately determined by subtracting the random background as shown in Fig.7*b, c*. The background curve is given by the function (8). This curve corresponds to the random distribution of sources within a circle. That is why we work with *circular events* and with the distribution of *angular separations* of the pairs.

3. The background level in the peak domain can be further reduced by the cuts on radial separation ΔL_{\max} .

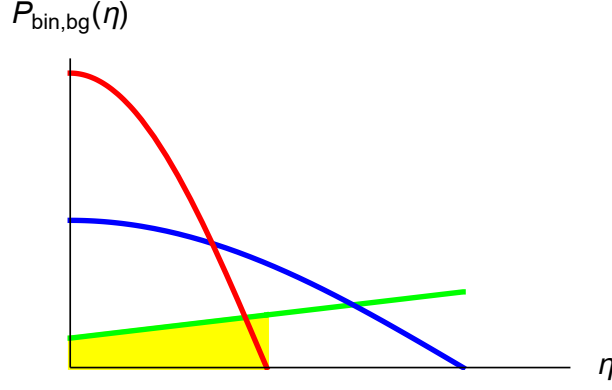


Figure 11. Distributions of true binaries P_{bin} (red and blue, which is wider, due to measurement errors) and background P_{bg} (green). Parameter η represent some selection parameter ($d_{ij}, \alpha_{ij}, \dots$). The numbers of the true binaries n_2 are given by the area under red and blue curves. Corresponding numbers of background pairs b_2 are given by the yellow area and the whole area under the green curve.

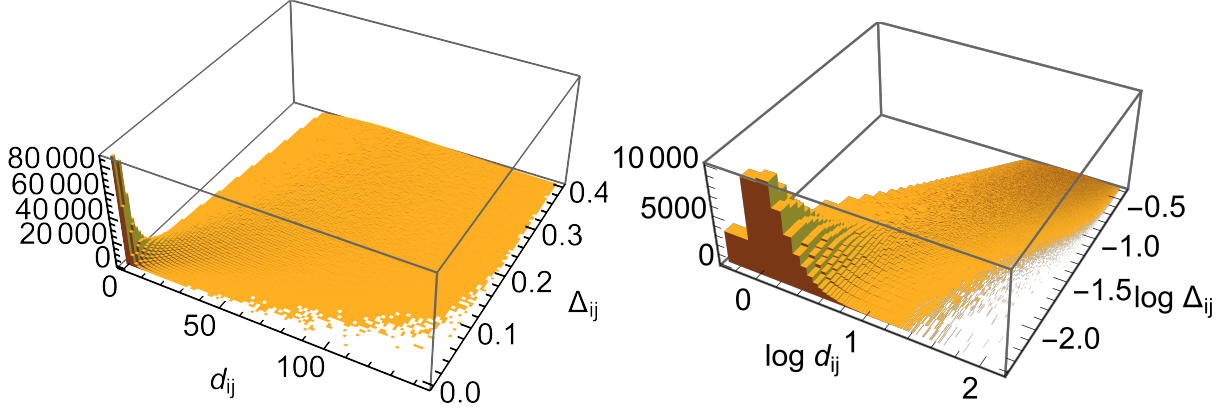


Figure 12. Correlation of angular separation d_{ij} [as] and projected distance Δ_{ij} [pc] for $\alpha \leq \alpha_c$. Left a right panel - linear and logarithmic scales. Binning: $1.44\text{as} \times 0.004\text{pc}$, $0.36\text{as} \times 0.001\text{pc}$.

4. The cuts α_c and $\Delta_{L_{\max}}$ reduce the background level, but does not change the shape of the corresponding background curve $q(\hat{\xi})$. This distribution, after the renormalization (10), is used for calculation of the probabilistic function β , which defines the selection quality.

2.4. Projected absolute separations, periods and masses of binaries

In Fig.12 we have shown an important correlation in the peak of binaries, where angular separation d_{ij} , as one would expect, strongly correlate with the projected distance Δ_{ij} that is calculated as

$$\Delta_{ij} = d_{ij} \frac{L_i + L_j}{2}. \quad (33)$$

Distribution of Δ_{ij} in the region of peak (windows **A** in Fig.8) is shown in Fig.13. In panels *b, c* we have shown distributions from subsets with higher rate of binaries. We observe that

$$\Delta_{ij} \lesssim 0.1 \text{ pc}, \quad (34)$$

which confirms our former result from 3D analysis. In panel *a* we observe presence of pairs, which contradicts this constraint. It is due to high rate of background pairs in this set. Note that nearby binaries with wider separation can be outside of our acceptance window **A**. In fact only candidates with separation

$$\Delta_{ij} \leq d_c L \approx 7 \times 10^{-5} L, \quad (35)$$

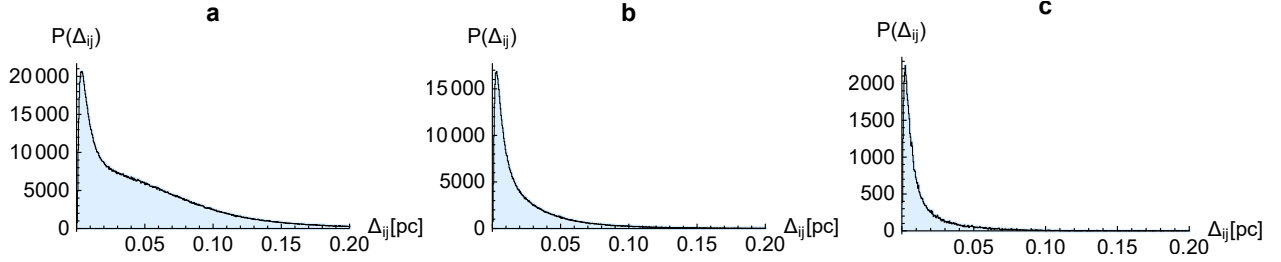


Figure 13. Projected distance Δ_{ij} of pairs in domains **A** of regions **R**₁ and **R**₂ defined in Fig.8. Panel *a*: all events, Panel *b*: enriched exposition, Panel *c*: only stars of magnitude $G \leq 15$. Binning: 0.0004pc.

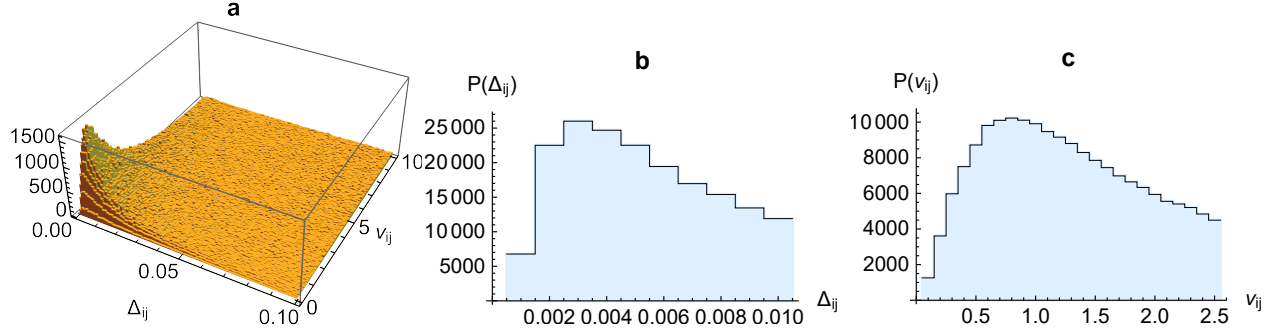


Figure 14. Panel *a*: Correlation of the transverse separation Δ_{ij} with the transverse velocity v_{ij} of orbital motion in region **R**. Panels *b, c*: Distributions of Δ_{ij} and v_{ij} in domain (37). Units: Δ_{ij} [pc], v_{ij} [km/s]. Binning: 0.001pc×0.1km/s, 0.001pc, 0.1km/s.

where L is average distance of the pair, are accepted.

Similarly as before (Zavada&Píška (2020)), we can estimate the projection of the orbital velocity of the binary as

$$v_{ij} = |\mathbf{u}_i - \mathbf{u}_j| \frac{L_i + L_j}{2}. \quad (36)$$

From the plot in Fig.14*a*, we can roughly estimate averages of the orbital periods and total masses of the binary systems. The binaries are accumulated in a peak very similar to that obtained earlier in 3D analysis. Very similar plot (with much lower statistics) can be obtained also for the subset of binaries with magnitude $G \leq 15$. If we take the sources roughly in the domain of half-width of the maximum (panels *b, c*)

$$\Delta_{ij} \leq 0.01 \text{ pc}, \quad v_{ij} \leq 2.5 \text{ km/s} \quad (37)$$

then in the approach described in (Zavada&Píška (2020)) we now obtain

$$\langle T \rangle \approx 4.2 \times 10^4 \text{ y}, \quad \langle M_{tot} \rangle \approx 0.65 M_\odot, \quad (38)$$

which is comparable with the previous approximate estimate ($8 \times 10^4 \text{ y}$, $0.8 M_\odot$) obtained in the cited paper. These numbers can also be compared with the results of the sample of thirty CPM (Common Proper Motion) pairs, which were discussed in (Duquenooy&Mayor (1991)), Table 4. These pairs represent wide binaries in the solar neighborhood, for which the table lists the parameters $\log T_i$ and masses M_{1i} and M_{2i} . We have calculated the mean values

$$\langle T \rangle = 10^{\langle \log T_i \rangle} \approx 2.6 \times 10^4 \text{ y}, \quad \langle M_{tot} \rangle = \langle M_{1i} + M_{2i} \rangle \approx 1.6 M_\odot, \quad (39)$$

which are also well comparable with our estimates above.

2.5. Wide trinarities and quaternaries

So far we have assumed the excess of close pairs (window **A**) is due to only binaries, which is correct only in a first approximation. A more detailed analysis indicates also a limited presence of multiple systems, trinarities and

region	m	enriched exposition				$G \leq 15$			
		N_m^A	b_m^A	n_m^A	β	N_m^A	b_m^A	n_m^A	β
R ₁	3	1,724	137	1,587	0.921	53	2	51	0.96
	4	12	0	12	1.	1	0	1	1.
R ₂	3	1,946	147	1,789	0.924	119	5	114	0.96
	4	10	0	10	1.	0	0	0	x
Σ	3	3,670	284	3,386	0.923	172	7	165	0.96
	4	22	0	22	1.	1	0	1	1.

Table 3. Statistics of trinary and quaternary candidates ($m = 3, 4$) in regions **R₁** and **R₂**. Table shows the numbers of candidates, estimated background and true trinaries and quaternaries (N_m^A , b_m^A , n_m^A), $\beta = n_m^A/N_m^A$.

quaternaries. To identify their candidates, we will generalize our criterion of binary candidates. For each pair in the candidate multiple system we require the same condition as for separation of binaries (20). Three stars create three separations, four stars create six separations. In Tab.3 we have shown statistics of events involving just one isolated trinary or quaternary candidate (N_m^A). The random background events (b_m^A) are obtained from the real events in which the local coordinates $\{x_i, y_i\}$ are replaced by random positions inside the same events. The difference $N_m^A - b_m^A$ represents the estimate of number of the true multiple systems n_m^A . The presence of multiple systems implies that the number of binary candidates N_2^A should be reduced by

$$\Delta N_2^A = 3N_3^A + 6N_4^A, \quad (40)$$

which gives $\approx 1.6\%$ in the set of enriched exposition.

For each triplet of stars inside the event we define the triangle separation as

$$d_{ijk} = \max(d_{ij}, d_{jk}, d_{ki}). \quad (41)$$

If $\alpha\beta$ are subscripts of the most separated pair, then the components of triangle separation are defined as

$$x_{ijk} = |x_\alpha - x_\beta|, \quad y_{ijk} = |y_\alpha - y_\beta|. \quad (42)$$

Distributions of these parameters are shown in Fig.15 together with the distributions corresponding to the background, which is generated by randomly distributed sources in the event. The high level of the background under the slight trinary peak at $d_{ijk} \lesssim 20$ as (upper panel left) is due to primarily by binaries. Each binary generates also excess of triangle separations. It is illustrated in Figs.16 and 17. In the first figure (left panel) we show the simulated distribution of separations of random sources with the admixture of extra close pairs. The parameters of this admixture (*probability* of close pairs and *width* of normal distribution of their separations) are set to reproduce distributions in the real events (right panel). Distributions of triangle separations obtained from the same set are shown in Fig.17. The last figure explains a high background under the trinary peak in upper panels of Fig.15.

Fig.8 and Tab.3 show that in the window **A(R)** of enriched exposition we have 511,998 binaries, 3,404 trinaries and 22 quaternaries. However, the total numbers are greater. The estimate based on the all events window (**A-D**) in upper panels of Fig.8 gives the total number of binaries roughly 1.5×10^6 . However, as we discussed in (Zavada&Pířka (2020)), part of them (mainly in windows **B,C**) may be an image of widening pairs that were less separated but weakly bound in the past.

3. CATALOGUE

In this section, we describe the catalogue of the multiple star candidates, which are selected with the use of the events defined by Tab.1. For the present version of the catalogue, we accept only the candidates from window **A(R)** of the enriched exposition defined in the middle part of Fig.8. So, the selected pairs satisfy the conditions of angular separation, collinearity and radial separation:

$$d \leq 15 \text{ as}, \quad \alpha \leq 15 \text{ deg}, \quad \Delta L \leq \Delta L_{\max}, \quad (43)$$

where ΔL_{\max} is defined in relation (30) for region **R₁** and in Tab.2 for **R₂**. We record:

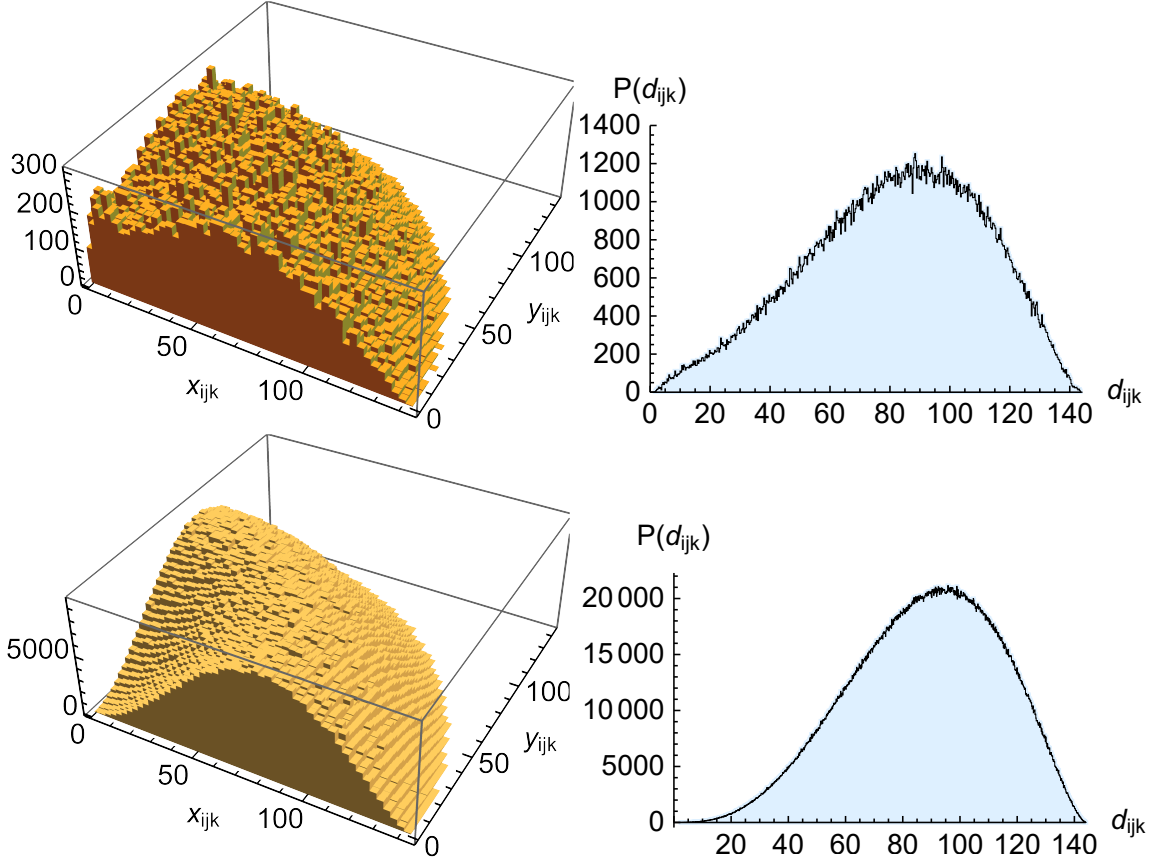


Figure 15. Distributions of angular separations x_{ijk}, y_{ijk} and d_{ijk} in trinary candidates. Upper panels show results from the region **R** (enriched exposition). The lower panels represent background. Unit: $x_{ijk}, y_{ijk}, d_{ijk}$ [as]. Binning: $2.88\text{as} \times 2.88\text{as}, 0.288\text{as}$.

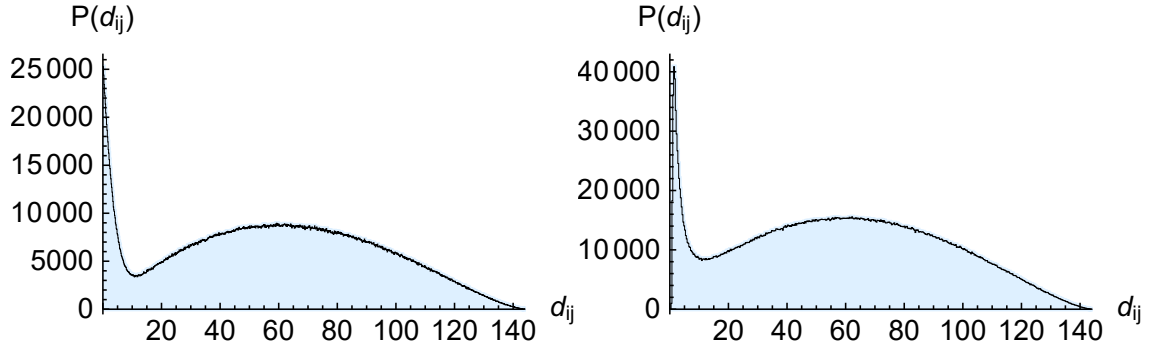


Figure 16. Distributions of angular separations d_{ij} . *Left:* Random sources with the admixture of close pairs. *Right:* Real event data from region **R** (enriched exposition). Unit: d_{ij} [as]. Binning: 0.288as .

1. Binary candidates: separate pairs that satisfies (43).
2. Trinary candidates: separate triplets of sources, where each pair (3 in total) satisfies (43).
3. Quaternary candidates: separate quaternions of sources, where each pair (6 in total) satisfies (43).

Examples of possible patterns in window **A** generated in one event are symbolically shown in Fig.18. We skip the events with empty window **A**. Pairs with the bar meet (43), pairs without the bar do not. Now we work with the patterns, where each source has at least one bar. According to the above definition, diagrams represent the candidates in the event: one binary (*a*), two binaries (*b*), one trinary (*c*), one quaternary (*d*). The rate of other combinations of candidates is negligible. Combinations that do not correspond to the defined candidates, such as diagrams *e*, *f*, also have very little weight. We skip them and accept only candidates *a-d* into the catalogue. The circle events cover only

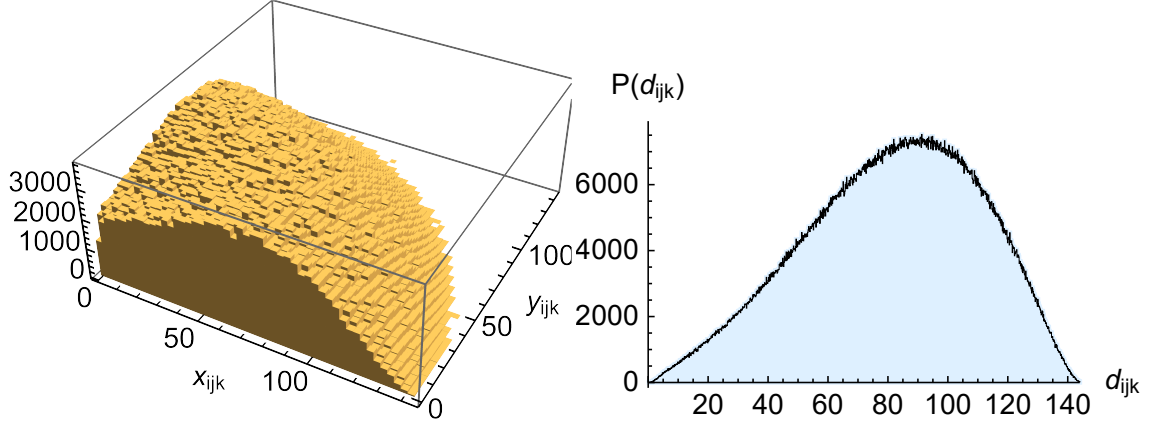


Figure 17. Distributions of angular triangle separations x_{ijk}, y_{ijk} and d_{ijk} for the same set of simulated events used in the previous figure. Unit: $x_{ijk}, y_{ijk}, d_{ijk}$ [as]. Binning: $2.88\text{as} \times 2.88\text{as}, 0.288\text{as}$.

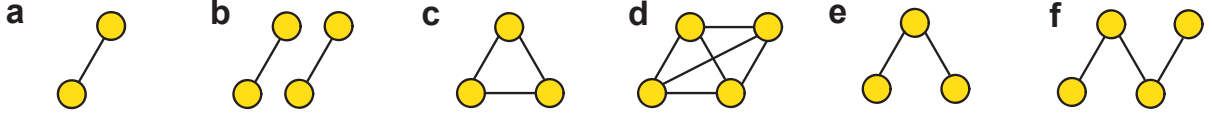


Figure 18. Examples of patterns relevant to the selection (rejection) of candidates for multiple stars.

m	N_m^A	β	n_m^A	Δn_m^A
2	900,842	0.733	660,317	696
3	5,282	0.923	4,875	67
4	30	1.	30	6

Table 4. Summary table of multiple stars in the window $\mathbf{A}(\mathbf{R})$ of enriched exposition.

part of the sky (corresponding to the fraction $\pi/4$). We also lose candidates between neighboring events when the pairs are split between the neighbors. To recover these losses, we work with modified coverage:

i) The event circles of radius 72as are replaced by squares of edge 144as with no gaps between them. In each square, we search for multiple star candidates.

ii) The procedure is repeated with the same squares centred in the corners and the edge centres of the former squares (we have 4 grids in total). Then the search results are merged, the summary data are given in Tab.4. The quality ratios $\beta = n_m^A/N_m^A$ are taken from the analysis of circle events with well defined background (Fig.8 and Tab.3). Now we can use them to estimate n_m^A and corresponding statistical errors

$$\Delta n_m^A = \beta \sqrt{N_m^A}. \quad (44)$$

It is seen the number of multiple systems decreases rapidly with their multiplicity:

$$\frac{n_3^A}{n_2^A} \approx 0.7\%, \quad \frac{n_4^A}{n_3^A} \approx 0.6\%. \quad (45)$$

In Fig.19 we have shown distribution of distances of all stars accepted to the catalog. Note that selection criteria exclude preferably the most distant sources from distribution in Fig.2. Obviously, the candidates of higher quality (but lower quantity) can be obtained from the catalog by reselection with more strict cuts (43).

The catalogue of selected candidates is represented by a matrix, which is defined as follows. Each row represents one star and there are the following data in the columns:

1-2: Group ID and Group size ($n = 2, 3, 4$) to match stars with the group they belong to.

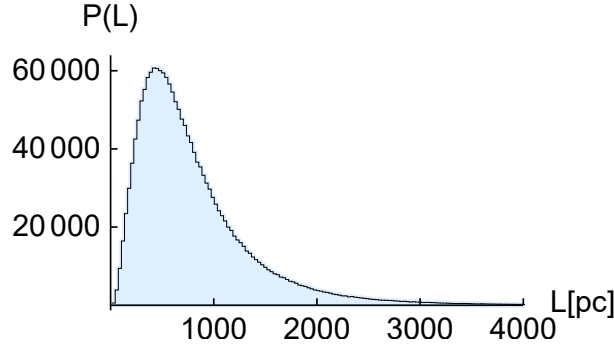


Figure 19. Distances of all candidate sources. Binning: 30pc.

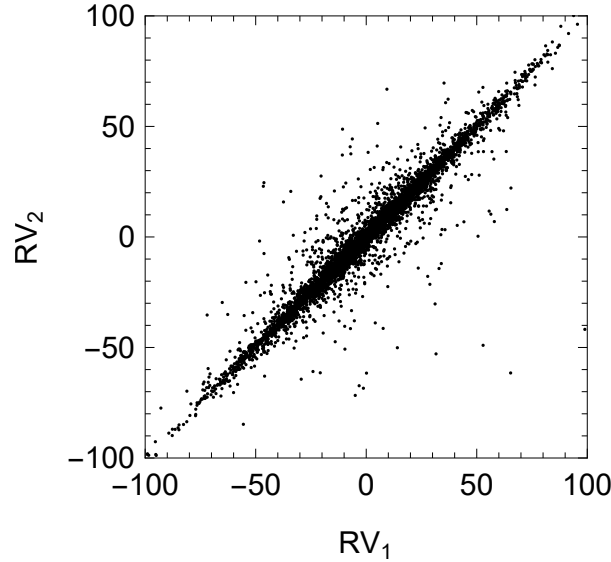


Figure 20. Correlation of radial velocities for 6469 pairs. Unit: [km/s].

3–96: Copy of the original entry for the star from *Gaia*-DR2 catalogue ¹, according to the documentation ².

97–98: Minimum and maximum angular separation of the star from other stars in the group [as].

99–100: Minimum and maximum projected physical separation (33) of the star from other stars in the group [pc].

The quality of our catalogue can be easily verified for brighter binaries, where the DR2 data includes radial velocities. The catalogue contains 6469 such pairs, only 16 of them involves a star with magnitude $G > 15$. In Fig.20 we show the correlation of both velocities, which confirms the common radial motion of the pairs. This result agrees very well with the same correlation obtained from the DR2 catalogue in (Andrews et al. (2018)) and (Sapozhnikov et al. (2020)).

4. COMPARISON WITH OTHER CATALOGUES

The catalogues of wide binaries (El-Badry et al. (2021); Hartman&Lépine (2020); Jiménez-Esteban et al. (2019); Zavada&Píška (2020)) and our present one are based on the selection defined by three parameters measured by the *Gaia*: angular position (separation), proper motion and parallax. However, catalogues differ in the choice of algorithm, which processes these variables. To illustrate, we will compare the algorithm used in this study (A1) with the algorithm used for the recent catalogue (El-Badry et al. (2021)) containing a comparable amount of binaries (A2).

i) angular separation

¹ http://cdn.gea.esac.esa.int/Gaia/gdr2/gaia_source/csv/

² http://gea.esac.esa.int/archive/documentation/GDR2/Gaia_archive/chap_datamodel/sec_dm_main_tables/ssec_dm_gaia_source.html

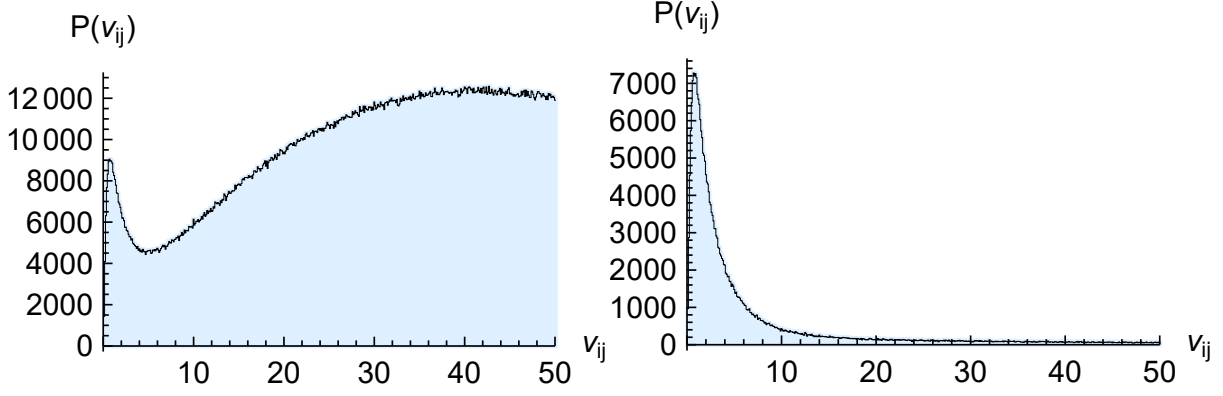


Figure 21. Distribution of velocities v_{ij} for all pairs (left) and for pairs in the peak (15) (right) in the region \mathbf{R}_1 (enriched exposition). Unit: v_{ij} [km/s]. Binning: 0.1 km/s.

This parameter is measured with a high accuracy. The presence of binaries generates a clear peak in its distribution at small separations. The random background in the events is exactly described by the function (8). The peak in angular separations is the basic signature of binaries in the algorithm A1.

From angular separation one can, with the use of parallax, calculate projected separation. Both parameters are strongly correlated. The cut on projected separations $\Delta \leq 1\text{pc}$ is applied in the algorithm A2. However, the question of the background is here more complex, see discussion below.

ii) proper motion

In algorithm A2, the difference of velocities v_{ij} (36) is limited by the cut

$$v_{ij} \leq v_{\max}. \quad (46)$$

The algorithm A1 is based on conditions (15), which define the domain of the peak with the high population of binaries (Fig.4). The algorithm includes an accurate calculation of the background under the peak. What are the velocities v_{ij} inside and outside this peak? The answer is given in Fig.21. The left panel shows the distribution of velocities for all pairs within the event, the peak at small v_{ij} corresponds to the binaries. The right panel shows the same distribution for the pairs in the peak domain. Corresponding pairs are mostly binaries, so the large velocities are strongly suppressed. The panel represents the distribution of the orbital motion projection. One can admit, the tail of distribution may still be contaminated with some background pairs. Alternatively, instead of our cut

$$\alpha_{ij} \leq \alpha_{\max} \quad (47)$$

it would be possible to set the cut (46). In the present study, we preferred (47), because the angle α_{ij} does not depend on the parallax, which has a large measurement error. For future analysis of the *Gaia* DR3 data, in which a more accurate parallax measurement is expected, we plan to try replacing (47) with (46), which can more effectively suppress the background.

iii) parallax

The parallax p or the distance $L = 1/p$ are determined with a large error, ΔL is usually larger than the expected binary dimension. Large radial separation does not necessarily mean that the pair is not true binary. However, a smaller radial separation (or difference of parallaxes) increases the probability that the pair is true binary. Therefore the algorithm A1 requires limited radial separation defined by (8) and Tab.2. Similarly, the A2 requires limited difference of parallaxes.

Finally, both algorithms similarly reject denser clusters of sources: event multiplicity $M > 25$ (A1) and number of neighbors > 30 (A2). In general, algorithms have a similar philosophy but differ in technical details.

A very important technical step is to define random background (A1) or equivalently the chance alignments (A2). In this respect, the two algorithms differ significantly. Let's make a comparison.

A1: The distribution of separations of random sources inside a circle is given exactly by formula (8). The shape of this curve does not depend on other parameters such as magnitude, the direction of proper motion or the parallax. The binary peak can be separated from the background described by this curve, see Sec.2.3 and examples in Figs.10

	N_{tot}	$N_{b>25}$	reference/DR
A1	900,842	900,842	this paper/DR2
A2	1,256,400	496,888	El-Badry et al. (2021)/EDR3
A3	93,898	55,319	Hartman&Lépine (2020)/DR2
A4	80,560	40,107	Zavada&Píška (2020)/DR2
A5	3,055	381	Jiménez-Esteban et al. (2019)/DR2
A6	9,977	5,546	Sapozhnikov et al. (2020)/DR2

Table 5. Numbers of the binary candidates in the compared catalogues.

	A1	A2	A3	A4	A5	A6
A1		343,302	39,031	24,949	59	2,862
A2	151,738\555,691		x	x	x	x
A3	54,530\861,469	x		28,312	85	7,290
A4	54,707\874,969	x	51,811\65,148		108	7,937
A5	2,979\900,765	x	2,967\93,810	2,937\80,442		11
A6	7,115\897,980	x	7115\897980	2,040\72,693	9966\3015	

Table 6. Comparison of catalogues A1 -A6 shows the numbers of identical N_{ij}^{iden} (above diagonal) and unique $N_i^{uniq} \setminus N_j^{uniq}$ (below diagonal) candidates.

and 10. The normalized background curve is

$$q(\hat{\xi}) \approx 8\hat{\xi} + \dots \quad (48)$$

for small $\hat{\xi}$ (peak region). The probability of finding binary in a selected subset is given by function β defined by ratio (25), examples are shown in Fig.10.

A2: From the *Gaia* EDR3 data input, there are produced two files involving pairs with seven parameters $\mathbf{x} = \{\text{angular separation, distance, parallax difference uncertainty, ...}\}$:

- a) Catalogue of candidates
- b) Catalogue of chance alignments (shifted catalogue)

The densities of pairs $N_{\text{candidates}}(\mathbf{x})$ and $N_{\text{chance align}}(\mathbf{x})$ in the seven-dimensional parameter space are approximated by the Gaussian kernel density estimates. The ratio of these approximations

$$\mathcal{R}(\mathbf{x}) = \frac{N_{\text{chance align}}(\mathbf{x})}{N_{\text{candidates}}(\mathbf{x})} \quad (49)$$

is the parameter, which provides classification of the quality of candidates: the low \mathcal{R} means a high probability that the candidate is true binary, as illustrated in Fig. 5 in El-Badry et al. (2021). In the right panel of this figure, we observe: the lower \mathcal{R} (and higher quality of the candidate) means stronger suppression of more separated pairs. It is the result, which correlates with the shape of probabilistic function β in A1. However, the ratio \mathcal{R} of both approximations does not strictly mean *probability*, which the authors admit.

We will compare the contents of the catalogues listed in Tab.5. We define three types of candidates for any two compared catalogues A_i, A_j :

- 1) unique - the candidate appears in only one catalogue (N_i^{uniq})
- 2) identical - the candidate appears in both catalogues (N_{ij}^{iden})
- 3) indefinite - cannot be decided, for example, two candidates from two catalogues have only one common star, or the pair in one catalogue is part of a greater system in another one.

The results of the comparison are shown in Tab.6 In the section above the diagonal, there are the numbers N_{ij}^{iden} , below the diagonal we have the numbers $N_i^{uniq} \setminus N_j^{uniq}$. In the catalogue A2, only such pairs can be used for comparison, where the IDs of both stars appear also in the *Gaia* DR2 data. We perform the comparison of A2 only with our catalogue (A1, $|b| > 25$ deg), so the other corresponding places in the table are empty (x). Unique candidates are

based on different selection conditions in A1 and A2. For example, in A2, the unique part is generated mostly by candidates with greater angular separation ($d > 15$ as) than is accepted in A1. On the other hand, A1 imposes much weaker constraints on parallaxes, which generate its unique part. That is why in Fig.19 we observe many candidates more distant than 1000 pc (upper limit in A2). The occurrence of trinary and quaternary systems is analyzed only in A1. So, the content of both independent catalogues is partly complementary and partly identical.

Our current analysis is limited to $|b| > 25$ deg because we have verified that in the dense region $|b| \leq 25$ deg, the efficiency of selection (ratio β^A) based on conditions (15) from the DR2 catalogue is even lower than in the region \mathbf{R}_2 . And additional cuts on radial separation (similar to Tab.2) are not sufficiently effective. With the expected DR3 data release, where higher accuracy of astrometric data (mainly of the parallax) is assumed, we plan to recalculate the selection of multiple stars in the full angular range (4π).

The content of our previous catalogue A4 has already been compared with the A5, which contains 3,055 binaries with magnitude $G \leq 13$ (Zavada&Přiska (2020)). Comparison A1 with A5 implies that only 381 of the A5-candidates belong to A1-region $|b| > 25$ deg and only about 60 of which meet selection criterion $d \leq 15$ as. As shown in Tab.6, similar comparisons were made also for other catalogues. In general, the only partial overlap of different catalogues is due to mainly different cuts in selections algorithms.

For example, the content of present catalogue A1 is compared with our previous version A4, where the binary candidates inside the surrounding cubic region $(400 \text{ pc})^3$ are recorded. The candidates from the previous catalogue that meet the conditions

$$|b| > 25 \text{ deg}, \quad d \leq 15 \text{ as} \quad (50)$$

should be present in the new catalog as well. There are 25,604 such candidates and we succeeded 24,949 of them to identify with binaries of the new catalogue. So, the misidentification rate is small, $\approx 2.6\%$. It can occur, for example, with the diagram in Fig.18e that is excluded for the new catalog, but still one pair can meet the criteria of the previous one. At the same time, within the part of the cubic region that is common to both catalogues, the number of binary candidates of the new catalogue is 79,771. It is $79,771/25,604 \approx 3$ times more, than the candidates in the previous one. This ratio proves high efficiency of the optimized method applied in the present analysis.

Our new catalogue A1 covers the region $|b| > 25$ deg up to the distance $\lesssim 3,000$ pc and contains about 10 times more candidates than the previous A4, which covered full 4π , but only up to $\lesssim 340$ pc. A total of almost 10^6 candidates are recorded in both merged catalogues. For more detailed comparison of the catalogues A1, A3, A4, A5 and A6, which are based on the *Gaia* DR2 data, we have created the merged catalogue. This catalogue is the list of pairs consisting of four items: order number of binary, mask 103456 denoting origin from A1,A3,A4,A5,A6 and two DR2 sources ID. The catalogues A1, A4 and the merged one are available in the csv form on the website <https://www.fzu.cz/~piska/Catalogue/>.

5. SUMMARY AND CONCLUSION

With the use of the optimized statistical method for analysis of 2D patterns we studied occurrence of wide multiple stars: binaries, trinary and quaternary systems. The candidates are selected using the astrometric data collected in the *Gaia*-DR2 catalogue. So, we have studied the pairs with angular separation wider than ≈ 0.5 as, which is present *Gaia* lower limit for resolution of two sources. Our present analysis covers the region of galactic latitude $|b| > 25$ deg and radial distance $L \lesssim 15,000$ pc. In this space we have analyzed about 1.3×10^7 circle events of diameter 144 as involving 7.5×10^7 sources. The circle shape is advantageous for calculation of the random background. The total number of processed sources with positive parallax is about 1.2×10^8 .

The analysis is focused on two basic parameters related to any pair of sources in the multiple systems: angular separation d and collinearity α of their proper motion. Distribution of these parameters is compared with distributions generated by the random background. The domain of the clear peak of binaries is limited by conditions (15) that serve as the cut for the selection of candidates. The exact knowledge of the background allows us to define probabilistic parameter β representing the quality of candidates. Additional condition, which is required for the radial separation ΔL , improves quality of candidates. After this selection (enriched exposition) the candidates are recorded in the attached catalogue. Total numbers of candidates of wide multiple stars in the region $|b| > 25$ deg are shown in Tab.4. The catalog is compared with some other catalogues of wide binaries selected from the *Gaia* data.

We have also shown that the results of the present 2D analysis are fully consistent with our previous 3D analysis of *Gaia* DR2 data. We confirm that the projection of wide binary orbit satisfies approximate relation (34). The average period and mass of the wide binary systems (38) are very similar to our previous estimates based on 3D analysis.

1 This work has made use of data from the European Space Agency (ESA) mission *Gaia* ([https://www.cosmos.esa.](https://www.cosmos.esa.int/gaia)
 2 [int/gaia](https://www.cosmos.esa.int/gaia)), processed by the *Gaia* Data Processing and Analysis Consortium (DPAC, [https://www.cosmos.esa.int/](https://www.cosmos.esa.int/web/gaia/dpac/consortium)
 3 [web/gaia/dpac/consortium](https://www.cosmos.esa.int/web/gaia/dpac/consortium)). Funding for the DPAC has been provided by national institutions, in particular the
 4 institutions participating in the *Gaia* Multilateral Agreement. The work was supported by the project LTT17018
 5 of the MEYS (Czech Republic). We are grateful to A.Kupčo for the critical reading of the manuscript and valuable
 6 comments. Further, we are grateful to J.Grygar for his deep interest and qualified comments and O.Teryaev for useful
 7 discussions with interesting ideas. We thank S.A. Sapozhnikov for providing the link to their catalogue that we used
 8 for comparison.

REFERENCES

- Andrews, Jeff J. et al. 2018 Res. Notes AAS 2 29
- Arenou, F., Luri, X., Babusiaux, C., et al. 2018, A&A, 616, A17
- Caballero, J. A. 2009, A&A, 507, 251
- Close, L. M., Richer, H. B., & Crabtree, D. R. 1990, AJ, 100, 1968
- Kareem El-Badry, Hans-Walter Rix, Tyler M Heintz, Monthly Notices of the Royal Astronomical Society, 2021;, stab323
- Kareem El-Badry and Hans-Walter Rix, Monthly Notices of the Royal Astronomical Society, 480, 2018, 4884
- Duquenois, A. and Mayor, M., 1991, Astron. Astrophys. 248, 485
- Gaia Collaboration (Brown, A. G. A., et al.) 2018, A&A, 616, A1
- Gaia Collaboration (Smart, R.L., et al.) 2021, A&A, 649, A6
- Godoy-Rivera, D., Chanamé, J., 2018, Monthly Notices of the Royal Astronomical Society, 479, 4440
- González-Santamaría, I., Manteiga, M., Machado, A. et al. 2020, A&A 644, A173
- Halbwachs J.L., 1986, Astron. Astrophys. Suppl. Ser. 66, 131
- Hartman, Zachary D. & Sébastien Lépine 2020, ApJS 247:66
- Hernandez, X., Cortés, R. A. M., Allen, Ch. & Scarpa, R. 2019, International Journal of Modern Physics D, 28, 1950101
- Jiménez-Esteban, F. M., Solano, E. & Rodrigo, C. 2019, AJ, 157, 78
- Oelkers, R. J., Stassun, K. G., & Dhital, S. 2017, AJ, 153,259
- Oh, S., Price-Whelan, A. M., Hogg, D. W., Morton, T. D., & Spergel, D. N. 2017, AJ, 153, 257
- Jorge Peñarrubia, Aaron D. Ludlow, Julio Chanamé, Matthew G. Walker, 2016, Monthly Notices of the Royal Astronomical Society: Letters, 461, L72
- Charalambos Pittordis, Will Sutherland 2019, Monthly Notices of the Royal Astronomical Society, 488, 4740
- Sapozhnikov, S. A., Kovaleva, D. A., Malkov, O. Yu. & Sytov, A. Yu. 2020, Astron. Rep., 756, 64
- Hai-Jun Tian, Kareem El-Badry, Hans-Walter Rix and Andrew Gould, 2020, ApJS 246:4
- Zavada P. & Píška K., 2018, A&A, 614, A137
- Zavada P. & Píška K., 2020, AJ, 159,33
- Ziegler C. et al. 2018, AJ, 156,259